Journal Pre-proof

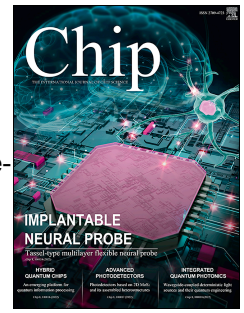

High-performance eight-channel system with fractal superconducting nanowire single-photon detectors

Zifan Hao, Kai Zou, Yun Meng, Jun-Yong Yan, Fangyuan Li, Yongheng Huo, Chao-Yuan Jin, Feng Liu, Thomas Descamps, Adrian Iovan, Val Zwiller, Xiaolong Hu

PII: S2709-4723(24)00005-4

DOI: https://doi.org/10.1016/j.chip.2024.100087

Reference: CHIP 100087

To appear in: *Chip*

Received Date: 27 December 2023

Revised Date: 4 February 2024

Accepted Date: 19 February 2024

Please cite this article as: Hao Z, Zou K, Meng Y, Yan JY, Li F, Huo Y, Jin CY, Liu F, Descamps T, Iovan A, Zwiller V, Hu X, High-performance eight-channel system with fractal superconducting nanowire single-photon detectors, *Chip*, https://doi.org/10.1016/j.chip.2024.100087.

High-performance eight-channel system with fractal superconducting nanowire single-photon detectors

Zifan Hao[a,b,f], Kai Zou[a,b,f], Yun Meng[a,b], Jun-Yong Yan[c], Fangyuan Li[c], Yongheng Huo[d], Chao-Yuan Jin[c], Feng Liu[c], Thomas Descamps[e], Adrian Iovan[e], Val Zwiller[e], Xiaolong Hu[a,b,g]

[a] *School of Precision Instrument and Optoelectronic Engineering, Tianjin University, Tianjin, 300072, China*
[b] *Key Laboratory of Optoelectronic Information Science and Technology, Ministry of Education, Tianjin, 300072, China*
[c] *State Key Laboratory of Modern Optical Instrumentation, College of Information Science and Electronic Engineering, Zhejiang University, Hangzhou, 300072, China*
[d] *Hefei National Research Center for Physical Sciences at the Microscale and School of Physical Sciences, University of Science and Technology of China, Hefei, 230026, China*
[e] *Department of Applied Physics, Royal Institute of Technology (KTH), SE-106 91 Stockholm, Sweden*
[f] *These authors contributed equally to this paper*
[g] *Corresponding author: xiaolonghu@tju.edu.cn*

Abstract

Superconducting nanowire single-photon detectors (SNSPDs) have become a mainstream photon-counting technology that has been used in various applications. So far, most multi-channel SNSPD systems, either reported in literature or been commercially available, are polarization sensitive, that is, the system detection efficiency (SDE) of each channel is dependent on the state of polarization of the to-be-detected photons. Here, we report on an eight-channel system with fractal superconducting nanowire single-photon detectors working in the wavelength range of 930-940 nm that all feature low polarization sensitivity. In a close-cycled Gifford-McMahon cryocooler system with the base temperature of 2.2 K, we install and compare the performance of two types of devices: (1) SNSPD, composed of a single, continuous nanowire, and (2) superconducting nanowire avalanche photodetector (SNAP), composed of 16 cascaded units of two nanowires electrically connected in parallel. The highest system detection efficiency (SDE) among the eight channels reaches $96^{+4}_{-5}\%$, with polarization sensitivity of 1.02 and dark-count rate of 13 counts per second. The average SDE for eight chan-

nels for all states of polarization is estimated to be $90 \pm 5\%$. We conclude that both the SNSPDs and the SNAPs can reach saturated, high SDE at the wavelength of interest, and the SNSPDs show lower dark- (false-) count rates while the SNAPs show better properties in the time domain. Using this system, we showcase the measurements of the second-order photon-correlation functions of light emission from a single-photon source based on a semiconductor quantum dot and from a pulsed laser. We believe that our work provides new choices of systems with single-photon detectors combining the merits of high SDE, low polarization sensitivity, and low noise that can be tailored for different applications.

Keywords: Superconducting nanowire single-photon detector, superconducting strip photon detector, fractal, quantum optics, photon correlation

Introduction

Superconducting nanowire single-photon detectors (SNSPDs) [1, 2], or, also referred to as superconducting strip photon detectors (SSPDs), have played vital roles in many classical and quantum photonic applications [3, 4, 5, 6, 7, 8]. Different than most commonly-used, meandering SNSPDs [9, 10], fractal SNSPDs feature low polarization dependence of their detection efficiency [11, 12, 13, 14, 15]. Up to now, all the fractal SNSPDs reported in literature were packaged and configured into single-channel systems [12, 13, 14, 15]. On the other hand, to our knowledge, multi-channel SNSPD systems, either reported in literature [16, 17, 18, 19] or been commercially available [20], are all polarization sensitive, and the multi-channel systems with SNSPDs that all feature low polarization-sensitivity remain unexplored. Such a high-performance multi-channel system would be very useful for multi-photon coincidence counting that is often used in experimental quantum photonics to characterize nonclassical light sources [17, 21] and quantum computation [3, 22, 23].

In this paper, we report on an eight-channel fractal SNSPD system in the wavelength range of 930-940 nm. This spectral range overlaps with the emission spectra of a category of single-photon sources based on III-V semiconductor quantum dots [24, 25, 26, 27]. In the system, we include 6 fractal SNSPDs [12] and 2 fractal cascaded superconducting nanowire avalanche photodetors (SNAPs) [14, 15]. By we carefully and strategically optimized

the design and nanofabrication of the devices, the highest SDE_{max} for the SNSPDs and the SNAPs are $96^{+4}_{-5}\%$ and $95 \pm 5\%$, respectively, at the base temperature of 2.2 K. The average SDE for eight channels for all states of polarization is estimated to be $90 \pm 5\%$. While both types of detectors show high SDE, the SNSPDs exceed in low dark-count rates (DCR) and therefore, low noise-equivalent power (NEP), whereas the SNAPs exhibit higher operating speed and better timing resolution. As a direct application, we use two channels to measure the second-order correlation functions of light emission from a single-photon source based on a semiconductor quantum dot and from a pulsed laser, and compare the results with those measured by two silicon single-photon avalanche diodes (SPADs).

Design and nanofabrication of the devices

We designed the detectors to the arced fractal geometry similarly to what have been reported previously [15] but with several important improvements to pursue extremely high SDE in the wavelength range of 930-940 nm. (1) We expanded the photosensitive area of each detector to allow more tolerance of the misalignment between the fiber and the detector and to ensure close to 100% coupling efficiency. To this end, the photosensitive areas of the SNSPDs and the SNAPs were designed to be 13.7 µm × 13.7 µm and 15.2 µm × 15.2 µm, respectively. We note that the fractal design of the SNAPs does not support an arbitrary size of the photosensitive area so that we cannot make the sizes of two types of detectors identical. (2) The thickness of the NbTiN film was still 9 nm [14], but we increased the width of the nanowire from 40 nm to 50 nm to reduce the difficulty in patterning and to increase the yield. Our consideration is that as the targeted wavelength is 930-940 nm, the energy of a single photon is larger than the energy of a photon in the telecommunication wavelength range of 1550 nm, a wider nanowire than what we used in the past [14, 15] could probably yield saturated detection efficiency. Fig. 1a and c present the false-colored scanning-electron micrographs (SEM) of the resulting fractal SNSPD and SNAP, respectively, and Fig. 1b and d present their equivalent circuitries. The process of nanofabrication is presented in METHODS. (3) For further enhancing optical absorptance, we increased the number of the pairs of the dielectric layers in the bottom DBR from 6 [14] to 8 pairs. Fig. 1e presents the designed microcavity composed of SiO_2 and Ta_2O_5 dielectric layers. The thicknesses of each SiO_2 layer in the DBR, each Ta_2O_5 layer in the DBR, and the SiO_2 defect layer are 152 nm,

106 nm, and 296 nm, respectively. The simulated intensity distribution of the light intensity along the y_D direction, assuming no NbTiN nanowires, is shown as the red line in Fig. 1e. Each detector was fabricated into the keyhole shape for self-aligned packaging with optical fiber [28] for top illumination. The photosensitive regions of the two types of detectors were designed and fabricated to be larger than the optical spatial modes, giving some tolerance of misalignment to ensure efficient optical coupling.

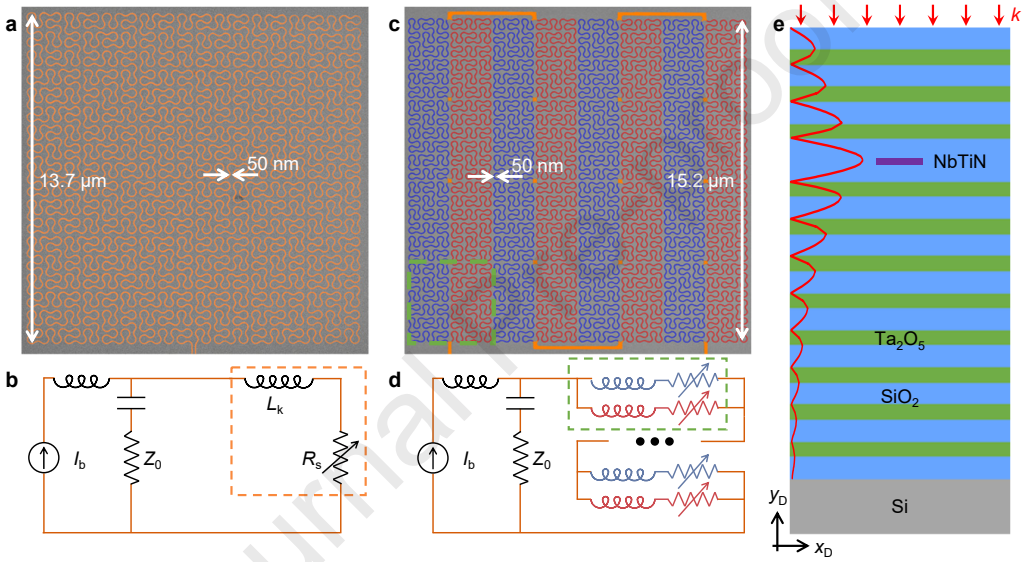

Fig. 1 Device structures of the fractal superconducting nanowire single-photon detector (SNSPD) and the superconducting nanowire avalanche photodetector (SNAP). a, False-colored scanning-electron micrograph of the fabricated SNSPD. The nanowire is designed and made into the arced fractal pattern, with the photosensitive area of 13.7 μm by 13.7 μm and the nanowire width of 50 nm. **b,** Equivalent circuitry of the SNSPD. **c,** False-colored scanning-electron micrograph of the fabricated SNAP. The detector is designed and made into a 16 cascaded 2-SNAP with the photosensitive area of 15.2 μm by 15.2 μm and the nanowire width of 50 nm. **d,** Equivalent circuitry of the SNAP. **e,** Schematics of the optical cavity structure, which is composed of the top distributed Bragg reflector (DBR) made of three pairs of alternating SiO_2 and Ta_2O_5 dielectric layers, the bottom DBR made of eight pairs of alternating dielectric layers, and the defect layer in between. The red line presents the simulated distribution of the light intensity in the microcavity, assuming the absence of the nanowire. The NbTiN nanowire is located at the position of the maximum intensity.

Characterization

All the measurements were performed by cooling the detectors to 2.2 K in a 0.1-W close-cycled Gifford-McMahon (G-M) cryocooler. For this particular cryocooler, we purchased the bare cryocooler and the compressor unit from Sumitomo, and designed and implemented the vacuum system with feedthroughs for optical fibers and electronic cables, the plate for mounting the chip packages as well as the radiation shields. The cooling curves are presented in Fig. 2. During the cooling process, we used power supply with the frequency of 60 Hz to increase the power of the compressor, and made the cooling process faster [29]. Specifically, we presented the cooling curves of the system with a single channel and eight channels configured, as shown in Fig. 2a. Additionally, zoom-in views are presented in Fig. 2b. The cooling speed of the system configured with a single channel is much faster than that of the eight-channel system, and it also reaches a lower minimum temperature due to the lower heat load. The single-channel system reaches a minimum temperature of 2.0 K after 3 hours of the cooling process, while the eight-channel system reaches a minimum temperature of 2.2 K after 6 hours.

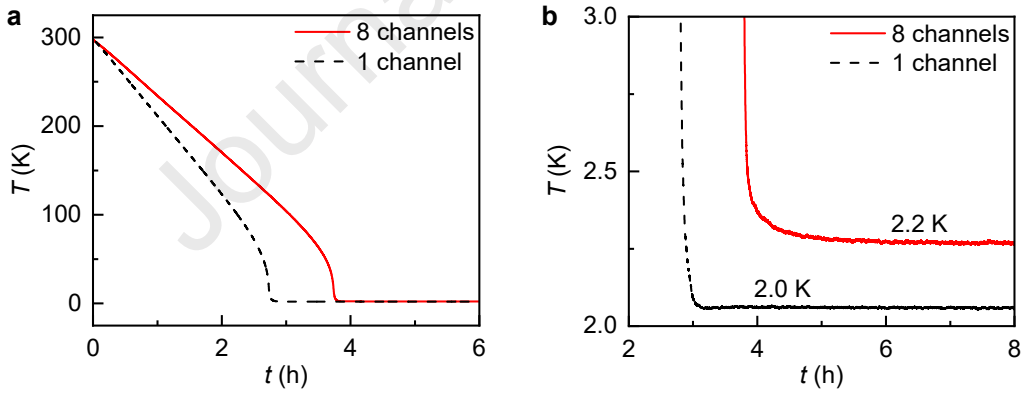

Fig. 2 Cooling-down curves of the Gifford-McMahon (G-M) cryocooler. **a,** Cooling-down curves of the G-M cryocooler with one channel and with eight channels. **b,** Zoom-in view of the curves in **a**.

We first measured the SDE and DCR/FCR of individual representative devices of the two types. For measuring SDE, we used the method based on time-correlated single-photon counting (TCSPC) [30] and used a SuperK with a monochromator as the light source [full width at half maxima

(FWHM) spectral width: 2 nm]. Low-noise RF amplifiers working at room temperature were used in this work. The schematic diagram of the experimental setup is presented in Fig. 3a.

Fig. 3b presents SDE_{max}, SDE_{min} and DCR for the SNSPD (channel C2). The switching current, I_{sw}, was 13.2 µA, and when $I_b > I_{sat} = 8.1$ µA, the SDE-I_b curves show saturated plateaus. We determined I_{sat} by fitting the measured SDE_{max}-I_b with an error function, taking a derivative that yielded a bell-like function, and finding the smallest I_b on the right of the peak making the normalized derivative less than 0.01. This I_b was treated as I_{sat}. DCR drops swiftly as decreasing the bias current from I_{sw}. As shown in Fig.3c, at the bias current of 9.4 µA, where NEP (calculated from SDE_{max} and DCR, NEP=$\frac{h\nu}{SDE_{max}}\sqrt{2DCR}$, where $h\nu$ is the photon energy [31, 32]) gets minimized, SDE_{max}=95 ± 5%, SDE_{min}=93 ± 5%, polarization sensitivity (PS)=1.02, and DCR=1.25 cps. The minimum NEP is 0.36×10^{-18} $W \cdot Hz^{-1/2}$.The relative error of the SDE measurement was estimated to be 5.3%, following the detailed analysis of various sources of uncertainties as in Ref. [15, 33]. We had corrected SDE by taking into account the optical reflection from the fiber facet when measuring optical power; the uncorrected values were SDE_{max}=98% and SDE_{min}=96%.

In comparison, Fig. 3d presents SDE_{max}, SDE_{min} and FCR for the SNAP (channel C4). The false counts include the dark counts and the afterpulses [34, 35, 14]. The switching current was 25 µA, and when $I_b > I_{sat} = 19.7$ µA, the SDE-I_b curves show saturated plateaus. FCR decreased as we decreased the bias current from I_{sw}, but when 13.8 µA< I_b <20.0 µA, and when further decreasing I_b, the detector was operating in the unstable regime and the FCR increased dramatically because of excessive afterpulses [34, 35, 14]. Therefore, As shown in Fig.3e, at the bias current of 20 µA, NEP (calculated from SDE_{max} and FCR, NEP=$\frac{h\nu}{SDE_{max}}\sqrt{2FCR}$) gets minimized, SDE_{max}=94 ± 5%, SDE_{min}=93 ± 5%, PS=1.02, and FCR=25.8 cps. The minimum NEP is 1.61×10^{-18} $W \cdot Hz^{-1/2}$. Therefore, the lowest FCR of the SNAP is a bit higher than the DCR of the SNSPD at the appropriate operating bias current.

We note that recent studies illustrated that the constrictions and bends are prone to generating dark counts [36, 37], however, here, the fractal SNSPD and the fractal SNAP containing plethora of bends in their photosensitive regions did not show excessive dark or false counts even fully biased. These observations indirectly evidenced the uniformity of the curved nanowires we patterned and fabricated. On the other hand, because the

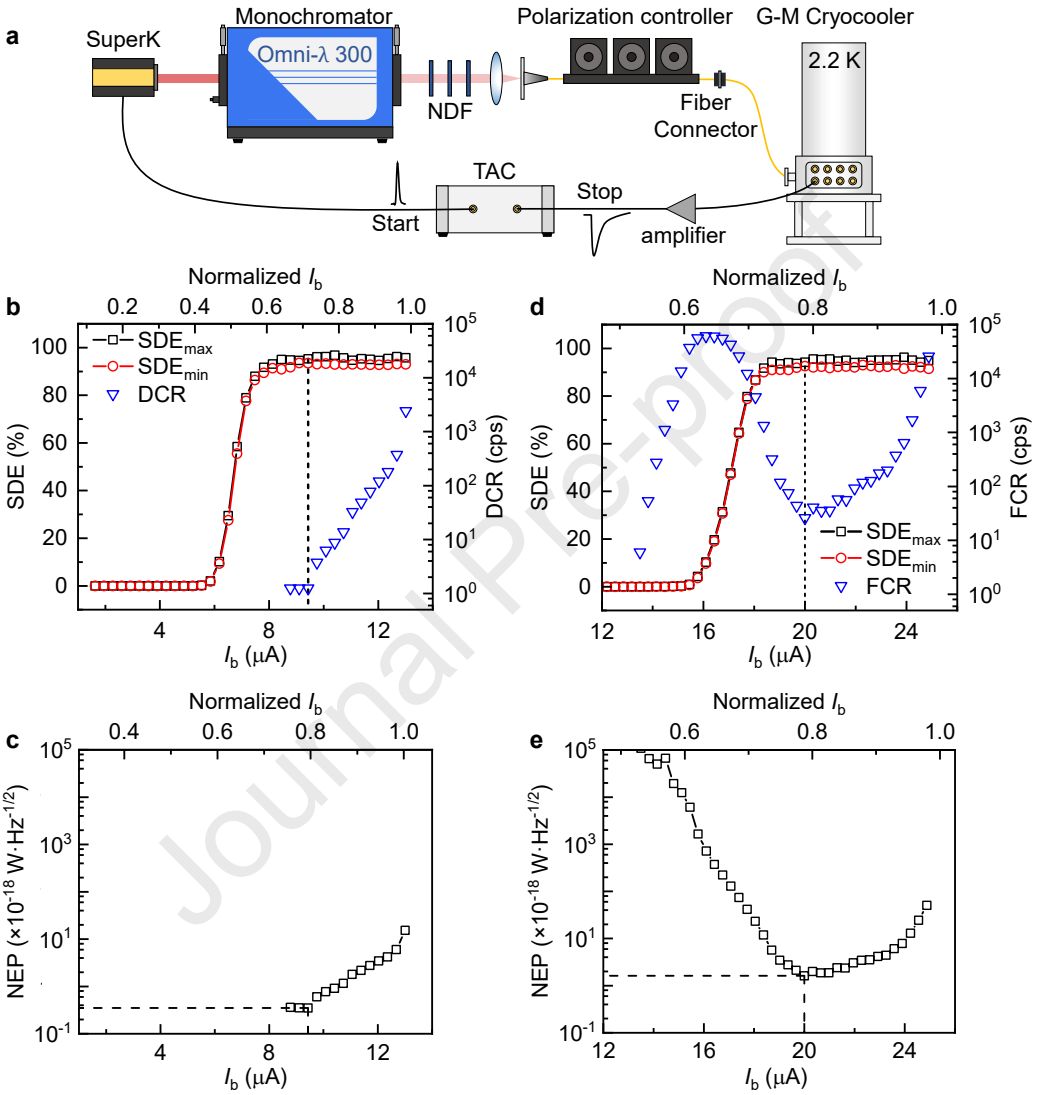

Fig. 3 Measured system detection efficiency and dark- or false-count rate. **a,** Schematic diagram of experimental setup. NDF, neutral density filter, TAC, time-to-amplitude converter. **b,** System detection efficiency and dark-count rate, as a function of the bias current, of a representative SNSPD (channel C2). **c,** Noise-equivalent power of the SNSPD. **d,** System detection efficiency and false-count rate, as a function of the bias current, of a representative SNAP (channel C4). **e,** Noise-equivalent power of the SNAP.

fractal geometry includes many U-turns and L-turns in the pattern of the nanowire, which is a key difference with the most commonly used meander SNSPDs, we think that the mechanism of the dark and false counts of the fractal SNSPDs and SNAPs is still quite elusive, and needs more detailed research.

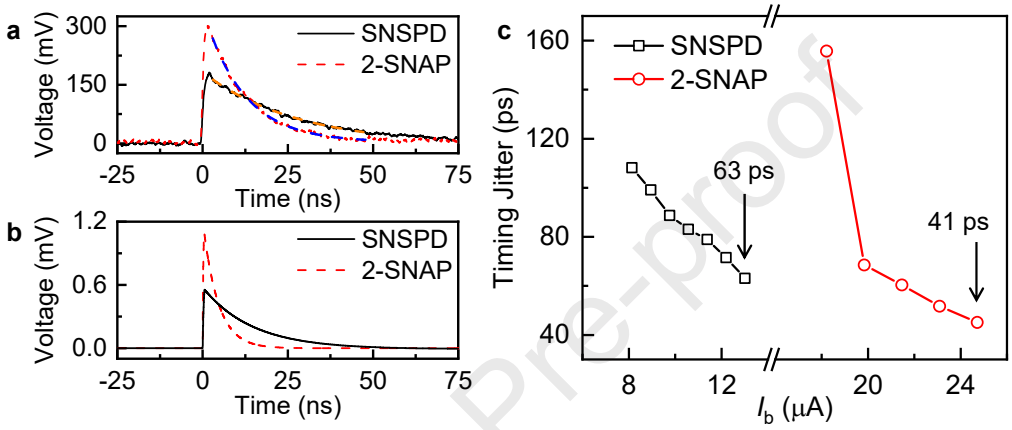

Fig. 4 Time-domain properties of the SNSPD and the SNAP. a, Output voltage pulses of the SNSPD (channel C2) and the SNAP (channel C4), after being amplified by a room-temperature RF amplifier. The exponential fittings of the falling edges show time constants of 18.0 and 7.9 ns for the SNSPD and the SNAP, respectively. **b,** Simulated output pulses of the SNSPD and the SNAP, without the RF amplifier, by thermoelectrical simulation. **c,** Measured timing jitter of the SNSPD and the SNAP, as functions of the bias current.

Figure 4 presents the time-domain properties of the SNSPD and the SNAP. Fig. 4a presents the oscilloscope traces of the output voltage pulses. The exponential-decay fittings show e^{-1} time constants of 18.0 and 7.9 ns for the SNSPD and the SNAP, respectively. Fig. 4b presents the traces simulated by thermo-electrical simulation, without considering the RF amplifier (See METHODS). The simulation reproduced the voltages pulses in terms of the relative amplitudes and the shapes. The simulated e^{-1} time constants were 14.5 and 4.4 ns for the SNSPD and the SNAP, respectively. The differences between the simulated and measured results are due, mainly, to the electronic filtering effect of the RF amplifier that was not taken into account in the simulation and the value of kinetic inductivity taken from Ref. [38], which may be slightly different than kinetic inductivity of the actual superconducting film used in our experiment. Fig. 4c presents the timing jitter

(FWHM of the time-delay histogram) as functions of I_b for the SNSPD and the SNAP. Timing jitter was measured with a low-noise RF amplifier working at room temperature and an oscilloscope with a real-time bandwidth of 4 GHz. Note that the measurements were conducted at 1560-nm wavelength using a femtosecond pulse laser and a high-speed photodetector with the bandwidth of 40 GHz. For the measurement of timing jitter, all detectors were pigtailed with SMF-28e optical fibers. The lowest timing jitter for the SNSPD and the SNAP were 63 and 41 ps, respectively.

We installed eight detectors in the cryocooler and performed complete characterization. Fig. 5a presents a photograph of the cold head with eight fiber-coupled packages installed on the self-designed stage. We measured the SDE_{max} and SDE_{min} of the eight detectors. Fig. 5b presents the measured SDE_{max} as functions of the wavelength of the incident light, with all the detectors biased at 97% of each I_{sw}. SDE_{max} of C3 peaked at 930 nm, and SDE_{max} of the remaining channels peaked at 940 nm. After determining the peak wavelength of each channel, we measured the SDE_{max} as functions of the I_b normalized to each I_{sw} at their peak wavelengths, as shown in Fig. 5c. All channels show saturated plateaus, and C4 and C8 are SNAPs, with relatively small bias region for the plateaus due to the unstable regime at low I_b. Fig. 5d summarizes the measured SDE_{max} and SDE_{min} of each channel. SDE_{max} of five channels exceed 90%, and all the channels' SDE_{max} exceed 80%. Each error bar represents 5.3% relative error. The average SDE for all states of polarization of the eight channels is estimated to be $90 \pm 5\%$, which is the average of the sixteen values of SDE_{max} and SDE_{min}. Fig. 5e presents the measured DCR or FCR at the I_b corresponding to the lowest NEP of each channel. Fig. 5f presents the e^{-1} time constant of the falling edges of output pulses. The lower kinetic inductance of the SNAPs, due to the parallel configuration of the nanowires, resulted in smaller e^{-1} time constants. Fig. 5g presents the measured timing jitter of each channel at 99% of its switching current. Among eight detectors, SNAPs showed better timing resolution (lower timing jitter) than SNSPDs.

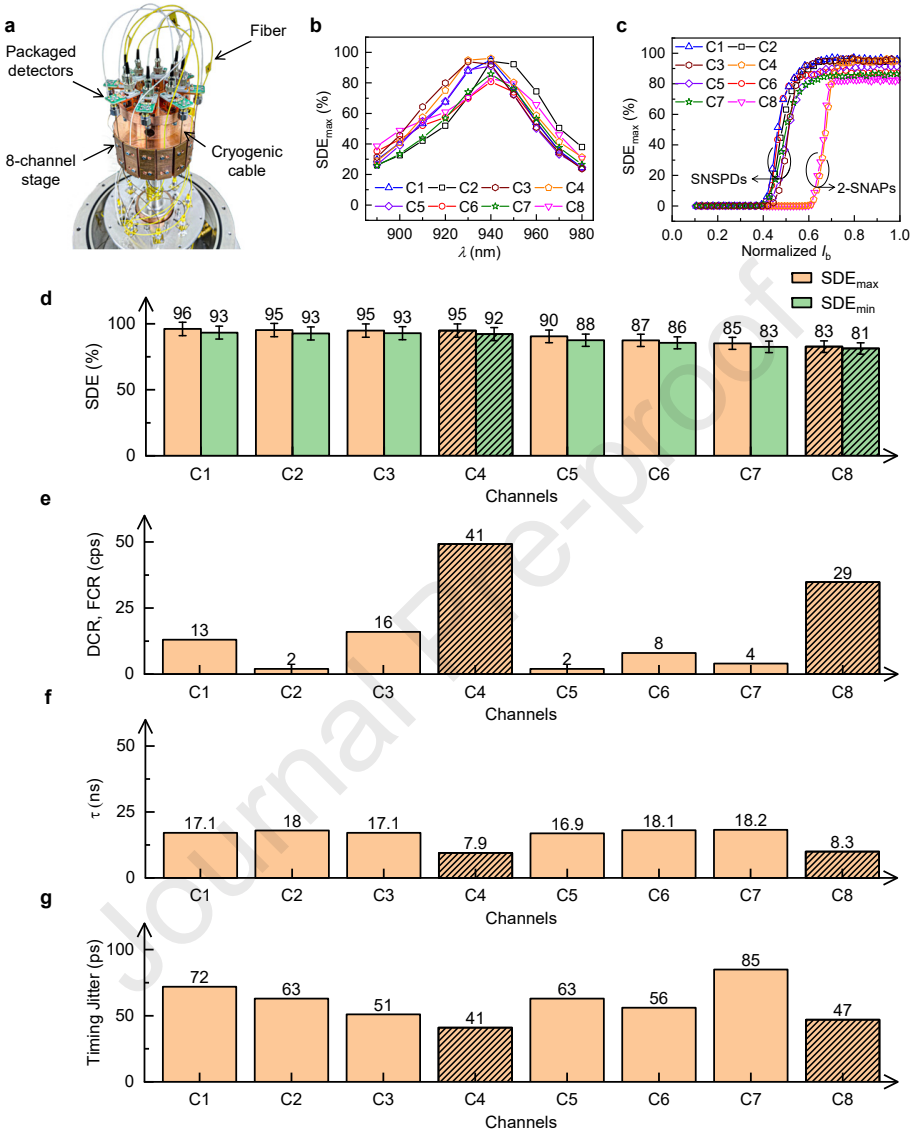

Fig. 5 Eight-channel fractal SNSPD system and the performance metrics. Channels C1, C2, C3, C5, C6, and C7 are SNSPDs, and Channels C4 and C8 are SNAPs. a, Photograph of the cold-head with eight packaged detectors installed. **b,** Measured SDE_{max} of eight channels as functions of the wavelength, λ. Each detector is biased at 97% of its switching current. **c,** Measured SDE_{max} of eight channels as functions of bias current normalized to each switching current. **d,** SDE_{max} and SDE_{min}. In **c** and **d**, C3 was measured at the wavelength of 930 nm and others were measured at 940 nm. **e,** DCR or FCR for each channel, corresponding to the lowest NEP of each detector. **f,** e^{-1} time constant of the falling edges of each channel's output pulses. **g,** Measured lowest timing jitter using a femtosecond pulse laser with a central wavelength of 1560 nm, the detectors were coupled with SMF-28e optical fibers when measuring timing jitter.

Measurements of photon-correlation functions

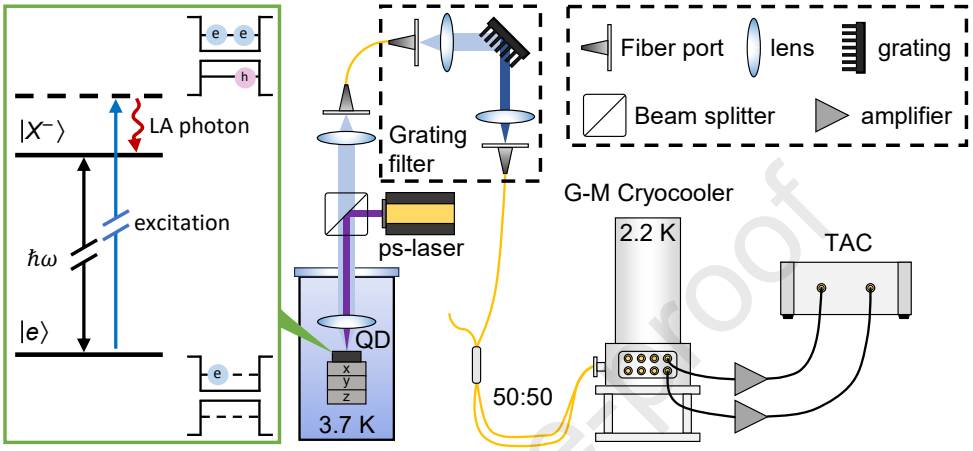

Fig. 6 Experimental setup for measuring second-order photon correlations, $g^2(\tau)$, of a single-photon source and a pulsed laser. TAC, time-to-amplitude converter.

As a demonstration of applications, we used two channels (C1 and C4) to measure the second-order correlation functions, $g^2(\tau)$, of the emission from a In(Ga)As/GaAs quantum dot (QD) and from a pulsed laser. Fig. 6 presents the experimental setup. The sample containing the quantum dots were cooled down to 3.7 K in another close-cycled cryostat. An individual quanutm dot was selected and excited by a picosecond pulsed laser and by longitudinal-acoustic (LA) phonon-assisted excitation scheme [39, 40]. The emission wavelength was centered at 887.1 nm, the excitation laser was blocked by a home-made grating-based spectral filter.

Figure 7 presents $g^2(\tau)$ measured by two SNSPDs and two silicon SPADs (purchased from Excelitas). For the emission from the QD, as presented in Fig. 7a and b, clear anti-bunching was observed and $g^2(0) = 0.0587$ measured by the SNSPDs. In comparison, $g^2(0) = 0.0609$ measured by the SPADs. For the pulsed laser, as presented in Fig. 7c and d, $g^2(0) = 0.968$ measured by the SNSPDs and $g^2(0) = 0.996$ measured by the SPADs. While the measured $g^2(\tau)$ were quite consistent by using the SNSPDs and by using the SPADs, from Fig. 7d, we can clearly see better timing resolution of the SNSPDs than that of the SPADs. In Fig. 7d, the full widths at half maxima of the $g^2(\tau)$

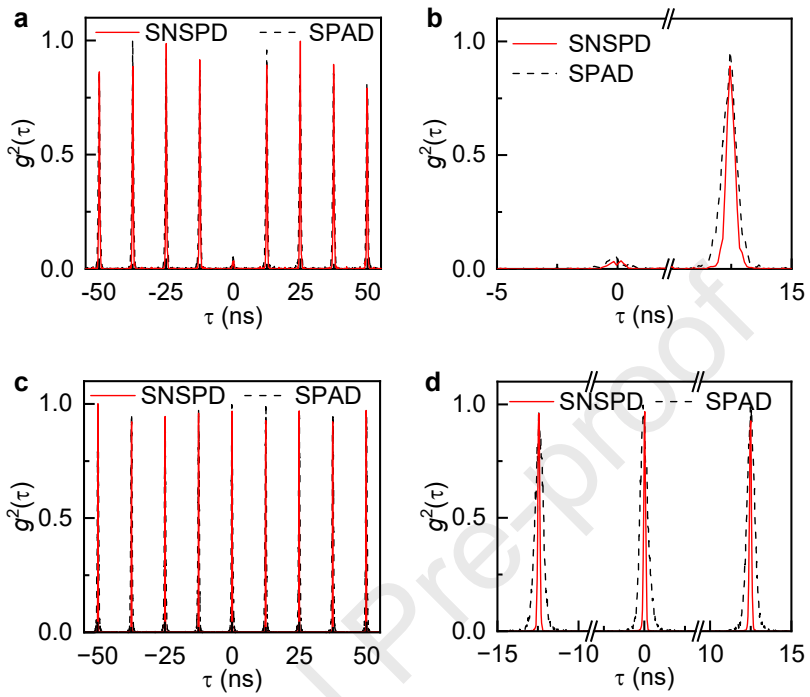

Fig. 7 Second-order photon-correlation functions, $g^2(\tau)$, of the light emission from a QD and a pulsed laser measured by two SNSPDs and two silicon SPADs. **a,** $g^2(\tau)$ of light emission from of the single-photon source, showing clear anti-bunching. **b,** A zoom-in view of **a**. **c,** $g^2(\tau)$ of light emission from of a pulsed laser with a FWHM of 6 ps. **d,** A zoom-in view of **c**.

peaks centered at $\tau = 0$ are 125 and 500 ps measured by the SNSPDs and the SPADs, respectively.

Conclusions

In conclusion, we have demonstrated an eight-channel system installed with fractal SNSPDs in the wavelength range of 930-940 nm that all feature low polarization sensitivity. The highest SDE is $96^{+4}_{-5}\%$, with 13 cps DCR. While both of the SNSPDs and the SNAPs achieved high SDE, the comparisons between them illustrate the strengths of each type – the former has lower DCR and therefore, lower noises, and the latter shows better properties in the time domain. Further improvement in the nanofabrication process can further enhance the yield of devices with high SDE and therefore, the comprehensive performances of the system. A better understanding of the dark

and false counts of the fractal SNSPDs and SNAPs is also needed. We believe that such a system would be useful in many quantum photonic applications involving multi-photon coincidence detection.

Methods

Nanofabrication of the chips: The steps of nanofabrication are similar to what were reported in Ref. [14]. Briefly, we deposited 8 pairs of SiO_2/Ta_2O_5 alternating layers and a half of SiO_2 defect layer by ion beam-assisted deposition (IBD) on a 4-inch, 300-µm-thick, double-side-polished silicon wafer. We sputtered a 9-nm thick NbTiN film by a reactive co-sputtering process at room temperature. Then we diced the wafer into dies with a dimension of 20 mm by 19 mm for the following process. We made the metallic contact pads and markers for alignment by optical lithography, followed by depositing a 10-nm-thick titanium and 100-nm-thick gold by e-beam evaporation. We lifted off unwanted metal by immersing the chip in acetone for 2 hours. We patterned the nanowires by scanning-electron-beam lithography, and a 50-nm-thick layer of hydrogen silsesquioxane (HSQ) was used as the negative-tone electron-beam resist. We transferred the pattern from the HSQ layer to the NbTiN layer by CF_4 and O_2 reactive-ion etching. We patterned the top reflector by optical lithography, followed by depositing another half SiO_2 defect layer of the micro-cavity, and 3 pairs of Ta_2O_5/SiO_2 bi-layers using IBD. Then, we did lift-off by immersing the chip in acetone for 2 hours. Finally, we etched the chip into the keyhole shape for self-aligned packaging. A 10-µm-thick layer of AZ 4620 was used as the photoresist. After patterning, we used inductively-coupled plasma etching to transfer the pattern to the stack. Finally, we removed the residual photoresist by immersing the chip in hot N-Methyl Pyrrolidone (NMP) at 95 °C for 1 hour.

Thermo-electrical simulation: We used one-dimensional thermo-electrical model to numerically simulate the transient responses of the SNSPD and the 2-SNAP by absorbing a single photon [41]. The values of kinetic inductance, normal-state resistance, bias current and switching current used in the simulation are 716 nH, 5.35 MΩ, 13.0 µA, and 13.2 µA, respectively, for the SNSPD, and are 220 nH, 2.43 MΩ, 24.8 µA, and 25.0 µA, respectively, for the 16 cascaded 2-SNAP. The switching current and the normal-state resistance were measured. The kinetic inductance L_k was calculated by $L_\mathrm{k} = l_\mathrm{k}\frac{L}{wd}$, where l_k, L, w, and d are kinetic inductivity, length, width, and thickness,

respectively. The value of the kinetic inductivity is from Ref. [38]. The length of the SNSPD and the 2-SNAP are calculated from the photo-sensitive area and the fill factor. The width and the thickness of the nanowires are 50 nm and 9 nm for both devices. The critical temperature is 9 K for both devices.

References

[1] G. N. Gol'tsman et al. Picosecond superconducting single-photon optical detector. *Appl. Phy. Lett.*, 79(6):705–707, 2001. https://doi.org/10.1063/1.1388868.

[2] X. Hu et al. Twenty-year research and development of SNSPDs: Review and prospects. *Laser Technology*, 46(1):1–37, 2022. https://doi.org/10.7510/jgjs.issn.1001-3806.2022.01.001.

[3] H. S. Zhong et al. Quantum computational advantage using photons. *Science*, 370(6523):1460–1463, 2020. https://doi.org/10.1126/science.abe8770.

[4] I. Esmaeil Zadeh et al. Superconducting nanowire single-photon detectors: A perspective on evolution, state-of-the-art, future developments, and applications. *Appl. Phy. Lett.*, 118(19), 2021. https://doi.org/10.1063/5.0045990.

[5] Y. Xiao et al. Superconducting single-photon spectrometer with 3d-printed photonic-crystal filters. *ACS Photonics*, 9(10):3450–3456, 2022. https://doi.org/10.1021/acsphotonics.2c01097.

[6] Y. Guan et al. Lidar with superconducting nanowire single-photon detectors: Recent advances and developments. *Opt. Laser Eng.*, 156:107102, 2022. https://doi.org/10.1016/j.optlaseng.2022.107102.

[7] F. Wang et al. In vivo non-invasive confocal fluorescence imaging beyond 1,700 nm using superconducting nanowire single-photon detectors. *Nat. Nanotechnol.*, 17(6):653–660, 2022. https://doi.org/10.1038/s41565-022-01130-3.

[8] H. Hao et al. A compact multi-pixel superconducting nanowire single-photon detector array supporting gigabit space-to-ground communications. *Light Sci. Appl*, 13(1):25, 2024. https://doi.org/10.1038/s41377-023-01374-1.

[9] D. V. Reddy et al. Superconducting nanowire single-photon detectors with 98% system detection efficiency at 1550 nm. *Optica*, 7(12):1649–1653, 2020. https://doi.org/10.1364/OPTICA.400751.

[10] P. Hu et al. Detecting single infrared photons toward optimal system detection efficiency. *Opt. Express*, 28(24):36884–36891, 2020. https://doi.org/10.1364/OE.410025.

[11] C. Gu et al. Fractal-inspired, polarization-insensitive superconducting nanowire single-photon detectors. In *Novel Optical Materials and Applications*, pages JM3A–10. Optica Publishing Group, 2015. https://doi.org/10.1364/IPRSN.2015.JM3A.10.

[12] X. Chi et al. Fractal superconducting nanowire single-photon detectors with reduced polarization sensitivity. *Opt. Lett.*, 43(20):5017–5020, 2018. https://doi.org/10.1364/OL.43.005017.

[13] Y. Meng et al. Fractal superconducting nanowire avalanche photodetector at 1550 nm with 60% system detection efficiency and 1.05 polarization sensitivity. *Opt. Lett.*, 45(2):471–474, 2020. https://doi.org/10.1364/OL.377228.

[14] Y. Meng et al. Fractal superconducting nanowires detect infrared single photons with 84% system detection efficiency, 1.02 polarization sensitivity, and 20.8 ps timing resolution. *ACS Photonics*, 9(5):1547–1553, 2022. https://doi.org/10.1021/acsphotonics.1c00730.

[15] K. Zou et al. Fractal superconducting nanowire single-photon detectors working in dual bands and their applications in free-space and underwater hybrid lidar. *Opt. Lett.*, 48(2):415–418, 2023. https://doi.org/10.1364/OL.481226.

[16] R. Cheng et al. Self-aligned multi-channel superconducting nanowire single-photon detectors. *Opt. Express*, 24(24):27070–27076, 2016. https://doi.org/10.1364/OE.24.027070.

[17] I. Esmaeil Zadeh et al. Efficient single-photon detection with 7.7 ps time resolution for photon-correlation measurements. *ACS Photonics*, 7(7):1780–1787, 2020. https://doi.org/10.1021/acsphotonics.0c00433.

[18] W. Zhang et al. Sixteen-channel fiber array-coupled superconducting single-photon detector array with average system detection efficiency over 60% at telecom wavelength. *Opt. Lett.*, 46(5):1049–1052, 2021. https://doi.org/10.1364/OL.418219.

[19] I. Craiciu et al. High-speed detection of 1550 nm single photons with superconducting nanowire detectors. *Optica*, 10(2):183–190, 2023. https://doi.org/10.1364/OPTICA.478960.

[20] Single Quantum: https://singlequantum.com;
ID Quantique: https://www.idquantique.com;
Photec: https://www.cnphotec.com/snspdsystem;
Scontel: https://www.scontel.ru/sspd;
Quantum Opus: https://www.quantumopus.com.

[21] F. Najafi et al. On-chip detection of non-classical light by scalable integration of single-photon detectors. *Nat. Commun.*, 6(1):5873, 2015. https://doi.org/10.1038/ncomms6873.

[22] Y. H. Deng et al. Gaussian boson sampling with pseudo-photon-number-resolving detectors and quantum computational advantage. *Phys. Rev. Lett.*, 131:150601, Oct 2023. https://doi.org/10.1103/PhysRevLett.131.150601.

[23] J. Gao et al. Quantum advantage with membosonsampling. *Chip*, 1(2):100007, 2022. https://doi.org/10.1016/j.chip.2022.100007.

[24] M. J. Stevens et al. Quantum dot single photon sources studied with superconducting single photon detectors. *IEEE J. Sel. Top. Quant.*, 12(6):1255–1268, 2006. https://doi.org/10.1109/JSTQE.2006.885088.

[25] K. Rivoire et al. Fast quantum dot single photon source triggered at telecommunications wavelength. *Appl. Phy. Lett.*, 98(8):083105, 2011. https://doi.org/10.1063/1.3556644.

[26] P. Senellart et al. High-performance semiconductor quantum-dot single-photon sources. *Nat. Nanotechnol.*, 98(8):083105, 2011. https://doi.org/10.1038/nnano.2017.218.

[27] J. Yan et al. Double-pulse generation of indistinguishable single photons with optically controlled polarization. *Nano Lett.*, 22(4):1483–1490, 2022. https://doi.org/10.1021/acs.nanolett.1c03543.

[28] Miller A. J. et al. Compact cryogenic self-aligning fiber-to-detector coupling with losses below one percent. *Opt. Express*, 19(10):9102–9110, 2011. https://doi.org/10.1364/OE.19.009102.

[29] Sumitomo RDK-101D(L) 4K Cryocooler Series: https://www.shicryogenics.com/product/rdk-101dl-4k-cryocooler-series/.

[30] S. Chen et al. Dark counts of superconducting nanowire single-photon detector under illumination. *Opt. Express*, 23(8):10786–10793, 2015. https://doi.org/10.1364/OE.23.010786.

[31] X. Hu. Efficient superconducting-nanowire single-photon detectors and their applications in quantum optics. PhD thesis, Massachusetts Institute of Technology, 2011. https://dspace.mit.edu/handle/1721.1/63073.

[32] J. Hu et al. Photon-counting optical time-domain reflectometry using a superconducting nanowire single-photon detector. *J. Lightwave Technol.*, 30(16):2583–2588, 2012. https://doi.org/10.1109/JLT.2012.2203786.

[33] J. Chang et al. Detecting telecom single photons with $99.5^{+0.5}_{-2.07}\%$ system detection efficiency and high time resolution. *APL Photonics*, 6(3):036114, 2021. https://doi.org/10.1063/5.0039772.

[34] F. Marsili et al. Single-photon detectors based on ultranarrow superconducting nanowires. *Nano Lett.*, 11(5):2048–2053, 2011. https://doi.org/10.1021/nl200514.

[35] F. Marsili et al. Afterpulsing and instability in superconducting nanowire avalanche photodetectors. *Appl. Phy. Lett.*, 100(11):112601, 2012. https://doi.org/10.1063/1.3691944.

[36] M. K. Akhlaghi et al. Reduced dark counts in optimized geometries for superconducting nanowire single photon detectors. *Opt. Express*, 20(21):23610–23616, 2012. https://doi.org/10.1364/OE.20.023610.

[37] X. Zhang et al. Geometric origin of intrinsic dark counts in superconducting nanowire single-photon detectors. *Superconductivity*, 1:100006, 2022. https://doi.org/10.1016/j.supcon.2022.100006.

[38] K. Zou et al. Superconducting nanowire multi-photon detectors enabled by current reservoirs. *Photonics Res.*, 8(4):601–609, 2020. https://doi.org/10.1364/PRJ.380764.

[39] J. H. Quilter et al. Phonon-assisted population inversion of a single InGaAs/GaAs quantum dot by pulsed laser excitation. *Phys. Rev. Lett.*, 114(13):137401, 2015. https://doi.org/10.1103/PhysRevLett.114.137401.

[40] S. E. Thomas et al. Bright polarized single-photon source based on a linear dipole. *Phys. Rev. Lett.*, 126(23):233601, 2021. https://doi.org/10.1103/PhysRevLett.126.233601.

[41] J. K. Yang et al. Modeling the electrical and thermal response of superconducting nanowire single-photon detectors. *IEEE Trans. Appl. Supercon.*, 17(2):581–585, 2007. https://doi.org/10.1109/TASC.2007.898660.

Funding

This work was supported by National Natural Science Foundation of China (62071322).

Acknowledgment

Portions of this work were submitted to OFC conference 2024 and were accepted as an oral presentation.

Declaration of Competing Interests

The authors declare no competing interests.

Declaration of interests

☒ The authors declare that they have no known competing financial interests or personal relationships that could have appeared to influence the work reported in this paper.

☐ The authors declare the following financial interests/personal relationships which may be considered as potential competing interests: